ARTICLE

Check for updates

Self-peeling of frozen water droplets upon impacting a cold surface

Wen-Zhen Fang [1,2,5], Fangqi Zhu[2,5], Lailai Zhu [3✉], Wen-Quan Tao[4] & Chun Yang [2✉]

Freezing of water droplets impacting a cold substrate is a commonly encountered circumstance impairing the performance and safety of various applications. Active methods of ice removal such as heating or mechanical means are energy intensive and inconvenient. Here, we report a passive ice removal method via harvesting the thermal-mechanical stress of ice, leading to the self-peeling of frozen water droplets upon impacting a cold substrate. We find that the frozen ice completely self-peels and is then easily removable from a cold hydrophobic surface whiles the ice exhibits cracking and remains firmly sticky to a hydrophilic surface. The peeling behaviors of frozen water droplets are then scrutinized by varying the subcooling degree, impact parameters and wettability. Moreover, we develop a theoretical model to characterize the peeling and bending behaviors of the ice and also provides a simple criterion to predict the occurrence of complete self-peeling, facilitating the design of anti-icing surfaces.

[1] Key Laboratory of Thermo-Fluid Science and Engineering of MOE, School of Energy and Power Engineering, Xi'an Jiaotong University, Xi'an 710049, China. [2] School of Mechanical and Aerospace Engineering, Nanyang Technological University, Singapore 639798, Singapore. [3] Department of Mechanical Engineering, National University of Singapore, Singapore 117575, Singapore. [4] Key Laboratory of Thermo-Fluid Science and Engineering, MOE, Xi'an Jiaotong University, Xi'an 710049, China. [5] These authors contributed equally: Wen-Zhen Fang, Fangqi Zhu. ✉email: lailai_zhu@nus.edu.sg; MCYang@ntu.edu.sg

cing is hazardous to the functionality of various engineering systems[1–7]. A common detrimental event occurs when water droplets become ice upon impacting a chilled surface[8–13]. Traditional active approaches for ice removal, such as by heating or mechanical means, require external energy input, and they are not only energy-consuming but can interfere the operation of application systems. Alternatively, exploiting the water repellency of superhydrophobic coatings offers a passive, low-weight, and inexpensive anti-icing method[14–20]. Typically, the impacting droplets rebound from a cold superhydrophobic surface immediately, decreasing the liquid-solid contact time[21–23]. Therefore, the cooling of droplets is reduced to below the threshold of triggering nucleation, enabling the droplets to escape before freezing[24–27]. Though being effective in certain conditions, this anti-icing mechanism would fail on sufficiently chilled surfaces because the heat loss from the droplets is enough to trigger their nucleation despite the decreased contact time, hence prohibiting their escape.

The failure of this passive icing protection results in irrepellable ice on deeply chilled surfaces, which might be alleviated by harnessing the thermal-mechanical stresses in the formed ice. Prior experiments indeed showed that such stresses in the solidified phase could deconstruct the solids and/or break the solid-surface bondage, illuminating a potential passive means of removing the solidified materials. For example, liquid metal droplets impinging on a cold surface commonly formed curling-up splats[28]; molten tin droplets impacting a silicon-wafer substrate underwent self-peeling to be detachable[29]; melted alkane droplets exhibited fractures and partial detachment[30], or delamination[31] upon hitting a chilled substrate. Likewise, water droplets impacting hydrophilic surfaces became ice that exhibited cracking[32] or broke into pieces[33]. We however are not aware of any experimental demonstration of using the thermal-mechanical stresses for passive ice removal.

In this work, we experimentally study the water droplets impacting cold surfaces with varying wettability. Different from the cracking behaviors on hydrophilic surfaces, we discover that the frozen water droplet self-peels from a sufficiently cold hydrophobic surface and is then easily removed by a breath of air, hence providing the experimental evidence to achieve the spontaneous delamination of ice via harnessing the thermal-mechanical stress. To reveal the underlying mechanism, we combine thermodynamics and elasticity theory to develop a model for describing the self-peeling behavior of ice, and we show that the model can capture the main features of the experiments. This model also offers a simple criterion to predict the occurrence of complete self-peeling.

Results

We conducted experiments inside a nitrogen gas-filled enclosed chamber. The experimental setup is illustrated in Supplementary Fig. 1. Individual deionized water droplets at room temperature were released above a copper substrate by its height H ranged from 9 to 90 cm. The chilled substrate was maintained at temperature T_s tuned from −10° to −47 °C. The substrate was treated to tune its static contact angle θ from 22° to 119°.

Freezing behaviors of impacting water droplets. We demonstrate in Fig. 1 from the side and top views, respectively, that the impacting droplet of $D_0 = 2.2$ mm exhibited self-peeling upon solidification on the coated, hydrophobic chilled substrate with a contact angle $\theta = 119°$ (Fig. 1a, c), in contrast to the ice cracking on a uncoated, hydrophilic counterpart with $\theta = 62°$ (Fig. 1b, d). The droplet impact height was $H = 45$ cm and the substrates'

temperature was $T_s = −43$ °C. In both cases, the droplet spread upon impacting onto the substrate at $t = 0$ ms and developed into a lamella sheet bounded with a rim. This structure reached a maximum diameter of $D_{max} \approx 8$ mm at $t = 1.8$ ms, as shown in Fig. 1b. Different from a droplet impacting a substrate at room temperature, it did not retract immediately due to the crystallization of supercooled water at the droplet-substrate interface. As the freezing propagated upwardly, the droplet became a mixture with water on the top of ice. The mixture evolved differently on the two substrates. On the hydrophobic surface, the ice disk started bending upwards at $t \approx 42.6$ ms and finally achieved self-peeling at $t \approx 49.6$ ms after the mixture was solidified completely. The ice bottom is detached from the surface, with a maximum defection of $\delta \approx 100$ μm at its edge. In the course of peeling, multiple concentric circular ridges arose from the water/ice-air interface due to the complex interaction between the droplet impact dynamics and the solidification[34–36]. Afterwards, applying a nitrogen gas flow of velocity ~2 m s⁻¹ could easily blow the ice away, indicating the self-peeling of ice on hydrophobic surfaces. Thus, this peeling behavior was termed complete peeling. In contrast, on the hydrophilic surface ($\theta = 62°$): the bottom of the water-ice mixture remained tightly adhered to the substrate during the whole process. The water/ice-air interface resembled a basin at $t = 17.2$ ms, which was thinner in the central region than the outer region. At $t \approx 17.6$ ms, ice cracking occurred, propagating from the center towards the edge.

A systematic examination revealed more diverse freezing behaviors when droplet impacts on cold surfaces with varying wettability. Figure 2a shows their dependence on the temperature difference $\Delta T = T_0 − T_s$ (between the freezing point $T_0 = 0$ °C and substrate temperature T_s) and $1 + \cos\theta$. Note that $1 + \cos\theta$ is linearly correlated with the water-substrate adhesive energy per unit area as $E_{w−s} = \gamma_{w−a}(1 + \cos\theta)$[37], where $\gamma_{w−a}$ is the surface tension between water and air. By assuming that the surface energies of water and ice are the same and they have similar interfacial energies at the solid surface, the work of adhesion for water can be approximated to the work of ice adhesion[38,39]. When decreasing ΔT from above 40 K to about 35 K, complete peeling (illustrated in Fig. 2b) from the hydrophobic surfaces ($\theta = 104, 110, 115$ and $119°$) transited to partial peeling—the ice self-peeled to a certain extent (Fig. 2c) but was irremovable under the applied gas flow; further lowering ΔT, the droplet became an ice disk without any peeling or cracking (Fig. 2d), which firmly stuck to the surface. A droplet impacting hydrophilic surfaces ($\theta = 62, 33$ and $22°$) exhibited the same state of no cracking or peeling when ΔT was below ~29 K, which agrees well with the results ($\Delta T = 27$ K) reported by Ghabache et al.[32]. This temperature threshold that separated cracking (Fig. 2e) or not was independent of the contact angle θ. Note that the ice cracking behaviors on hydrophilic surface were also reported when $\Delta T \leq 57$ K [33]. Importantly, they claimed that both the cracking and delamination were coexisted on the hydrophilic surface when ΔT increases to around 60 K, which was out of the temperature range we explored here.

These behaviors (cracking or peeling) of the frozen water droplets are determined by a competition among the thermal contraction of ice, cohesion among ice molecules, and adhesion between the ice and substrate. Chilled by a much colder substrate, the ice disk was subject to a rapid thermal contraction in the radial direction. This contraction was resisted by the ice cohesion or ice-substrate adhesion. Here, ice cohesive/adhesive energy are the work required to break the bond and form two new surfaces, i.e., the cohesive energy to create two new surfaces of ice while the adhesive energy to create new surface of substrate and ice. Thus, the cohesive and adhesive energy can then be quantified by the surface energy of ice γ_i
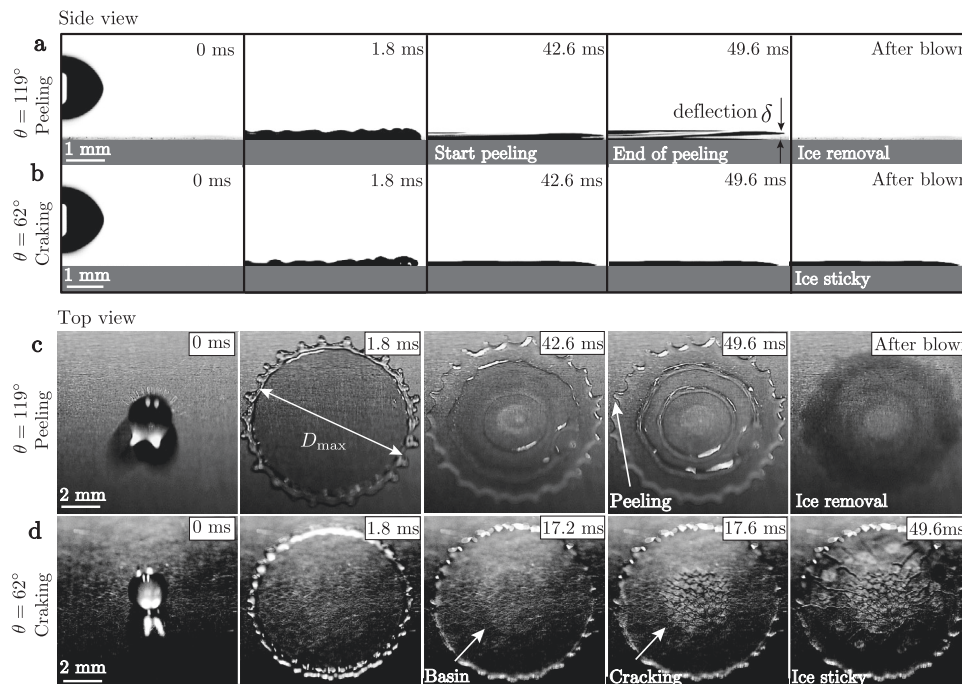
Fig. 1 Self-peeling and cracking of frozen water droplet. Side view (**a**, **b**) and top view (**c**, **d**) of a water droplet of diameter $D_0 = 2.2$ mm at room temperature released from height $H = 45$ mm impacting two copper substrates at temperature $T_s = -43$ °C: a coated substrate with a contact angle $\theta = 119°$ (**a**, **c**) and an uncoated counterpart with $\theta = 62°$ (**b**, **d**). The droplet was frozen into an ice disk of diameter $D_{max} \approx 8$ mm upon impact, and thereupon: when $\theta = 119°$, it self-peeled and thus was removed by a nitrogen gas flow at a speed of ~2 m s^{-1}; whereas when $\theta = 62°$, it underwent cracking and remained firmly attached to the substrate. See Supplementary Movie 1 and 2 for the details of peeling dynamics from side and top views, respectively.
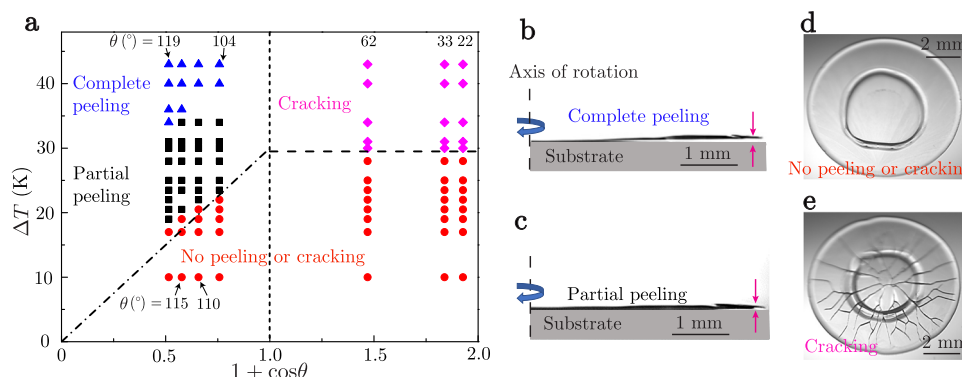

Fig. 2 Freezing behaviors of impacting water droplets. a Different behaviors of the impacting droplets released from $H = 45$ cm depending on the temperature difference $\Delta T = T_0 - T_s$ and surface wettability $1 + \cos\theta$: complete peeling (triangles), partial peeling (squares), no peeling or cracking (circles) and cracking (diamonds); these behaviors are illustrated by (**b-e**), respectively. Here, T_0 and T_s denote the freezing temperature and substrate temperature, respectively; $\cos\theta$ is the contact angle of surfaces.

and substrate γ_s, respectively. The former, $\gamma_i \approx 0.11$ J m^{-2} [40] remained almost constant among the temperature range in this study. However, γ_s significantly depends on the surface treatment and influenced the behaviors of ice. On the hydrophilic substrates, $\gamma_s \approx 1.8$ J m$^{-2} \gg \gamma_i$ [41], *viz.*, adhesion prevailed over cohesion. Hence, breaking the ice (cracking) was more energetically favorable than peeling itself from the substrate (against adhesion) when the subcooling degree ΔT increases. Besides, this argument together with the independence of γ_i on the surface also explains why the critical temperature ΔT above which cracking occurs does not vary with θ as shown in Fig. 2a. In contrast, on the coated, hydrophobic substrates, $\gamma_s \approx 0.02$ J m$^{-2} \ll \gamma_i$ [42] indicating a much weaker adhesive energy than the cohesive energy, which drove the ice to opt for peeling other than cracking (against cohesion). This reason also implies that the critical values of ΔT to trigger ice peeling on

hydrophobic surfaces generally increase with $1 + \cos\theta$ within the scope of this study. This trend agrees with the findings by Meuler et al. [43] that the ice adhesion strengthen increases linearly with $1 + \cos\theta$ on nominally smooth surface.

Thermal-mechanical model. Both the cracking and peeling behaviors of ice are driven by the thermal stresses resulting from the its contraction constrained by the substrate. Herein, we focus on developing a thermal-mechanical model to characterize the peeling process that might act as a key enabler for passive ice removal. We model the freezing water droplet as a two-layer cylinder of height h_0 comprising a water film above an ice disk (see Fig. 3a). Balancing the diffusive heat flux through the ice and its freezing rate, the evolving thickness $h(t) = \sqrt{2\lambda\Delta T t/(\rho_i L)}$ of
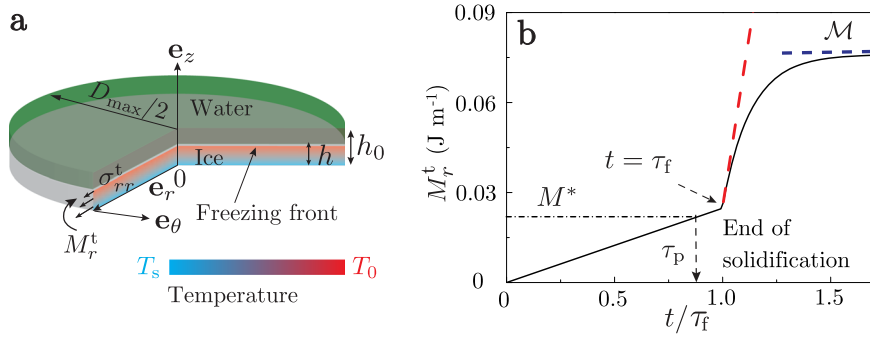
Fig. 3 Thermal-mechanical model. a The idea model of a freezing impacting droplet—a water film above a frozen ice disk (with maximum diameter D_{max}) whose temperature varies vertically ($\mathbf{e}_z$) from T_s at the substrate to T_0 at the freezing front. The thermal stresses (σ_{rr}^t) arise from the ice contraction constrained by the substrate. **b** Thermal elastic moment density M_r^t versus time t/τ_f, comprising a freezing period $t \leq \tau_f$ (Eq. (4)) and a post-frozen period $t > \tau_f$, where τ_f denotes the freezing time. We assume that when M_r^t exceeds the critical adhesive moment density M^*, the ice starts peeling. The time of peeling occurrence is denoted as τ_p. Here, $T_s = -40\,°C$. The red dashed line indicates the linearized moment density (Eq. (5)) when $t \to \tau_f^+$; the blue dashed line corresponds to the asymptotic value of M_r^t (i.e., $\mathcal{M}$) when $t \to \infty$.

the ice disk is derived[32], where ρ_i, λ, and L denote the ice's density, thermal conductivity, and latent heat, respectively, $\Delta T = T_0 - T_s$ and t denotes the time. Setting $h(\tau_f) = h_0$ implies the freezing time $\tau_f = \rho_i L h_0^2/(2\lambda\Delta T)$ when the water was completely frozen. Strictly speaking, $h(t)$ should depend on the temperature T_b at the droplet' bottom in contact with the substrate, other than that T_s at the bottom of the substrate. Here, we assume $T_b \approx T_s$ because the characteristic diffusion time in the copper substrate is smaller than the freezing time of droplet by one to two orders (see Supplementary Note 1). Besides, the sensible heat of water droplet is neglected here since it is much smaller compared to the latent heat.

The thermal stresses in the ice are determined by the distribution and evolution of the temperature, which we derive here by using the cylindrical coordinate system (r, θ, z) motivated by axisymmetric observations. Assuming its horizontal uniformity, we solve $T(z, t)$ governed by the one-dimensional heat equation $\partial_t T = \kappa \partial_{zz} T$, where κ is the thermal diffusivity of ice and the subscripts denote the partial differential with respect to t and z, respectively. We first realize that Stefan number $St = C_p\Delta T/L$ as the ratio of thermal diffusion timescale to freezing timescale is within $(0.05, 0.27)$ in our experiments, implying that the thermal diffusion is much faster than the ice solidification. Hence, in the freezing period $t \leq \tau_f$, we consider a quasi-steady distribution of temperature and accordingly solve $\partial_{zz} T = 0$ subject to $T(0, t) = T_s$ and $T(h(t), t) = T_0$[32], obtaining the linear temperature profile,

$$\frac{T(z, t) - T_s}{\Delta T} = z/h, \quad t \leq \tau_f. \quad (1)$$

After the completely frozen of water droplet, the temperature in the ice continues to cool down until reaching uniform. In this post-frozen period $t > \tau_f$, we assume that the top boundary is adiabatic since the thermal conductivity of air is two orders lower than that of ice and employ separation of variables to solve the transient heat diffusion equation with the adiabatic top boundary condition $\partial_z T(h_0, t) = 0$, acquiring

$$\frac{T(z, t) - T_s}{\Delta T} = \sum_{j=1}^{\infty} (-1)^{j+1} \frac{2\sin(\beta_j z)}{(\beta_j h_0)^2} \exp\left[-\kappa\beta_j^2(t - \tau_f)\right], \quad t > \tau_f, \quad (2)$$

where β_j is the j-th root of $\cos(\beta h_0) = 0$ (see Supplementary Note 1). Since the temperature variation in the post-frozen period is free of phase change, it evolves rapidly to become uniform (see

Supplementary Fig. 3). Consequently, the thermal stresses mainly originate in this stage, which will be demonstrated later (Fig. 3b).

Using Kirchhoff-Love plate theory[44] to describe the elastic deformation of the ice disk, we calculate the rr component of thermal stress tensor as $\sigma_{rr}^t = E\alpha[T(z, t) - T_0]/(\nu - 1)$ (see Supplementary Note 3), where E, ν, α are the Young's modulus, Poisson's ratio, thermal expansion coefficient of ice, respectively. The resulting thermal elastic moment density (per unit azimuthal length) is

$$M_r^t(t) = \int_0^h \sigma_{rr}^t z\,\mathrm{d}z = \frac{E\alpha}{\nu - 1} \int_0^{h(t)} [T(z, t) - T_0] z\,\mathrm{d}z. \quad (3)$$

Substituting Eqs. (1) and (2) into Eq. (3), we computed $M_r^t(t)$ and depicted it in Fig. 3b: in the freezing period $t \leq \tau_f$,

$$M_r^t(t) = \frac{1}{3(1 - \nu)} E\alpha(\Delta T)^2 \frac{\lambda t}{\rho_i L}, \quad t \leq \tau_f, \quad (4)$$

namely, M_r^t linearly grows with time t; after complete solidification ($t > \tau_f$), M_r^t rapidly increases with t and then reaches an asymptotic limit $\mathcal{M} = M_r^t(t \to \infty) = E\alpha\Delta T h_0^2/[2(1 - \nu)]$ (see Supplementary Note 1). In the early-time limit $t \to \tau_f^+$, we derive the linearized moment density

$$M_r^t(t) = \frac{E\alpha}{1 - \nu} \Delta T \left[h_0^2/6 + \kappa(t - \tau_f)\right], \quad t \to \tau_f^+, \quad (5)$$

as represented by the red dashed line in Fig. 3b.

Peeling and bending behaviors of ice. We infer that ice peeling occurs at $t = \tau_p$ when the growing elastic moment density M_r^t reaches a critical value M^* representing the ice-substrate adhesive energy density (per unit azimuthal length). Assuming that peeling occurs before complete solidification, viz., $\tau_p \leq \tau_f$, we use Eq. (4) to obtain the peeling time

$$\tau_p = \frac{3(1 - \nu)\rho_i L}{E\alpha\lambda} M^* \frac{1}{(\Delta T)^2}, \quad (6)$$

which scales inversely with $(\Delta T)^2$. This assumption is verified *posteriori* by Fig. 4a showing the experimentally measured τ_p versus ΔT for droplets of different sizes ($D_0 = 2.2$ mm, $D_0 = 2.8$ mm, $D_0 = 3.2$ mm), where most data agrees with the scaling law. Note that M^* in Eq. (6) scales as $\pi D_{max}\Gamma$, where Γ denotes the interfacial toughness which represents the bonding energy between ice and substrate. Thus, we plot the y-axis of Fig. 4a with τ_p/D_{max} and find that all the data well collapse into one single curve.
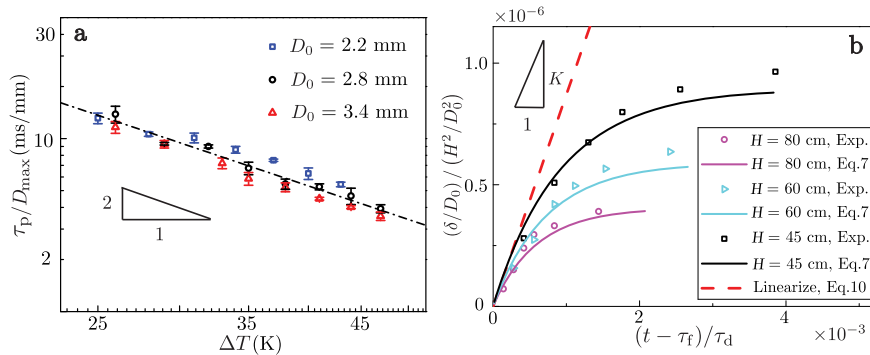
Fig. 4 Peeling and bending behaviors of ice. a The time of peeling appearance τ_p versus temperature difference ΔT for droplets with different sizes (initial diameters $D_0 = 2.2, 2.8, 3.4$ mm) released from height $H = 45$ cm, well following the scaling law $\tau_p \propto \Delta T^{-2}$ (Eq. (6)). Here, error bars denote the standard deviations among three tests and D_{max} is the maximum spreading diameter. **b** Post-frozen evolution of the scaled maximum ice deflection (δ) of a droplet with $D_0 = 2.2$ mm when $\Delta T = 40$ K. Here, the data are obtained on the surface with $\theta = 119°$. τ_f and τ_d are the freezing time and characteristic diffusion timescale, respectively. Note that the average values of δ among three measurements are used to calculate the scaled deflection, and there detailed variations are shown in Supplementary Fig. 5.

As shown in Fig. 1a, ice bending occurred after the peeling process was initiated. We hereby study this bending behavior by examining the early time ice deflection $w(r, t)$ at the radial position $r \in [0, D_{max}/2]$. Regarding the ice bottom (constrained by the substrate) as the neutral plane, we derive $w(r, t) = [M_r^t - M^*]r^2/[2B(1 + \nu)]$ (see Supplementary Note 3), where the flexural rigidity $B = Eh_0^3/[3(1 - \nu^2)]$. The maximum deflection δ that occurs at the edge $r = D_{max}/2$ is

$$\delta(t) = [M_r^t - M^*]D_{max}^2/[8B(1 + \nu)], \quad (7)$$

where $D_{max}/D_0 = c_0 We^{1/4}$ is found by fitting the experimental data at $\Delta T = 40$ K with Weber number defined as $We = 2\rho_w D_0 gH/\gamma_{w-a}$, in which ρ_w denotes the density of water and g is the gravitational acceleration; here $c_0 \approx 0.87$ (see Supplementary Note 2 and Supplementary Fig. 4) less than $c_0 \approx 1$ for iso-thermal droplet impacting[45,46] stemmed from the increased viscosity of colder water [24] or solidification[47] that prohibited droplet from spreading. Now we assume again that peeling occurs before the full solidification, namely, $\tau_p \leq \tau_f$. Substituting Eq. (5) into Eq. (7) and using the relation between D_{max} and D_0, we obtain the early-time ($t \rightarrow \tau_f^+$) evolution of $\delta(t)$ upon ice solidification,

$$\frac{\delta(t)}{D_0} = \bar{\delta}_f + K \frac{(t - \tau_f)}{\tau_d} \left(\frac{H}{D_0}\right)^2, \quad t \rightarrow \tau_f^+, \quad (8)$$

with the coefficient

$$K = \frac{81}{16} c_0^8 \left(\frac{g\rho_w D_0^2}{\gamma_{w-a}}\right)^2 \alpha\Delta T. \quad (9)$$

Here, $\tau_d = D_0^2/\kappa$ is the diffusion timescale and $\bar{\delta}_f = \delta(\tau_f)/D_0 = \frac{3}{8}\frac{D_{max}^2}{D_0 h_0}\left(\frac{\alpha\Delta T}{6} - \frac{M^*(1-\nu)}{Eh_0^2}\right)$.

We show a direct measurement of δ in Supplementary Fig. 5 and the scaled $\frac{\delta}{D_0}/\left(\frac{H}{D_0}\right)^2$ versus $(t - \tau_f)/\tau_d$ in Fig. 4b for droplets of $D_0 = 2.2$ mm released from different heights when $\Delta T = 40$ K. When $t = \tau_f$, the data imply $\delta \approx 0$, indicating that the deflection occurred during τ_p and τ_f is negligible and most deflections occur in the post-frozen period. This observation allows us to invoke the assumption $\bar{\delta}_f = \delta(\tau_f)/D_0 = \delta(\tau_p)/D_0 = 0$, leading to

$$\frac{\delta(t)}{D_0}/\left(\frac{H}{D_0}\right)^2 = K \frac{(t - \tau_f)}{\tau_d}, \quad t \rightarrow \tau_f^+. \quad (10)$$

This scaling relation is described by the red dashed line in Fig. 4b, which well captures the experimental trend. Note that by directly substituting the numerical expression of M_r^t during the post-frozen period (see Supplementary Eq. 6) into Eq. (7), we can obtain the evolution of ice deflection δ after peeling. As shown in Fig. 4b, it reasonably agree with the experimental data.

Finally, we scrutinize the freezing behaviors of the impacting droplet on hydrophobic surfaces by systematically varying the releasing height H of the droplet, temperature difference ΔT and contact angle θ (see Supplementary Fig. 6 for the detailed peeling behaviors at every test), and find that a larger ΔT and higher H would promote the complete peeling of ice. To quantitatively describe their effects on the peeling results, we identified a general variable—the ice disk's bending curvature κ_c that is theoretically determined from ΔT and H in every test. The upper limit of the scaled curvature $\kappa_c D_0$ can be calculated by considering the maximum thermal elastic moment $\mathcal{M}$ (see Fig. 3b) that drives ice bending and neglecting the adhesion that prohibits bending

$$\kappa_c D_0 = \frac{\mathcal{M}}{[B(1 + \nu)]} = \frac{3D_0}{2h_0}\alpha\Delta T \propto \Delta T H^{1/2}. \quad (11)$$

As shown in Fig. 5, the calculated $\kappa_c D_0$ can be used an indicator that demarcates complete peeling and partial peeling. Complete or partial peeling occurs when $\kappa_c D_0$ is above or below a threshold ≈ 0.03 that weakly increases with $1 + \cos\theta$, offering an easy way to forecast the icephobicity of coated surfaces. Together with the results shown in Supplementary Fig. 6, we can conclude that a more hydrophobic surface (within the scope of this study) promotes complete peeling by decreasing the threshold. Note that the model assumes that the ice disk has a constant bending curvature, which may deviate from the partial peeling situation where the center of ice is stuck on surface. Such deviation would not lead to a large error due to the small deflection during bending.

Discussion

In this work, we find that the freezing behaviors of frozen water droplet highly depend on the surface wettability: cracking on the hydrophilic surfaces while self-peeling on the hydrophobic surfaces. A more hydrophobic surface is favored due to its lower strength of ice adhesion, and thus a superhydrophobic surface seems promising. However, as pointed out by Varanasi et al.[48], the superhydrophobic surfaces show increased ice adhesion over the smooth surfaces due to the substrate textures. Besides, the
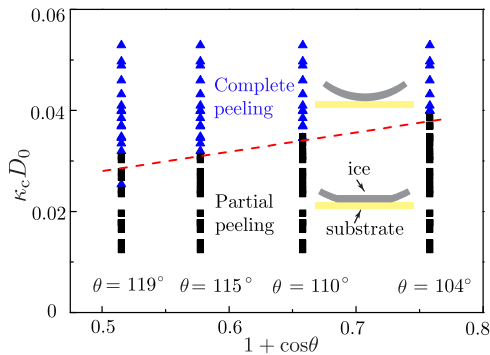
Fig. 5 Bending curvatures to distinguish complete peeling or partial peeling. Scaled bending curvature $\kappa_c D_0$ of the completely (triangles) or partially (squares) peeled ice on hydrophobic surfaces versus $1 + \cos\theta$, where κ_c is the curvature, D_0 is the initial diameter of droplets and θ is the contact angle. Here, $\kappa_c D_0$ is computed by Eq. (11) and the peeling behaviors are obtained from temperature difference $\Delta T \in (31, 43)$ K and height $H \in (9, 80)$ cm. The detailed peeling behaviors at every ΔT and H are shown in Supplementary Fig. 6.

penetration of impacting droplets into the textures[24] would affect the droplet dynamics and peeling process. The detailed peeling behaviors on the superhydrophobic surfaces remain to be further explored, and was not pursued here. In this work, all the copper-based substrates are well polished with surface roughness $S_a \leq 0.1\,\mu m$, and the surface contact angle is limited to 119°.

Although frosting on surfaces is expected at low temperatures, its growth is a random and uncontrollable process that can affect the surface condition before impact. Thus, we use the nitrogen-controlled atmosphere to prevent the frosting so as to ensure that the droplet impacts the same 'clean' surface on every single test. However, the frosting on surface may affect the ice peeling behaviors. How the frosting, especially the frosting thickness, affects the peeling behaviors needs further systematically study.

In summary, we have experimentally revealed different modes —cracking, sticking to the surface, and complete or partial self-peeling of a frozen droplet upon impacting a cold surface. We find that the freezing behaviors of impacting droplets (cracking or peeling) are dependent on the wettability and the underlying mechanisms are elucidated by comparing the relative strength of thermal-mechanical deformation, cohesion, and adhesion. The observed complete self-peeling of ice allows it to be easily delaminated from the surface, providing, to the best of our knowledge, the first experimental demonstration of passive ice removal by harnessing its thermal-mechanical stresses. We then explore the peeling behaviors by varying the subcooling degree ΔT, impact parameters and wettability and have developed a thermal-mechanical model that not only predicts the inverse relation between the peeling time and the square of ΔT, but also captures the early-time ice bending process. This model also yields a simple criterion to distinguish the complete peeling from partial peeling of the ice. The phenomenon of self-peeling-enabled ice removal, as well as the corresponding mechanistic insights revealed here, will facilitate the design of ice protective surfaces[49] and other passive anti-icing technologies[50].

Methods

Sample Surfaces. We prepared seven copper-based substrates via different technical processes. Their properties, including the contact angle θ, surface energy γ_s, and arithmetic mean roughness S_a, were listed in Supplementary Table 1. Before surface treatment, all the substrates were well polished using the same type of sandpaper. The roughness measurement also showed that the surfaces are 'smooth' enough, with small variations in roughness ($0.04\,\mu m < S_a < 0.1\,\mu m$). Such little variations are caused by the surface coating, and thus we did not discuss the roughness effect on the observed freezing behaviors.

For substrates No. 1 ~ No. 3, the polished copper was coated with a thin layer of Polytetrafluoroethylene (PTFE) by dip coating in the different mass fraction of PTFE solution. Specifically, by dipping it into a solution with 12.1 wt% PTFE dispersion in deionized water, the copper plate was covered by a 340 nm PTFE film, resulting the substrate No. 1 with a contact angle of $\theta = 119 \pm 1.2°$. Using another 3.0 wt% PTFE dispersion produced the substrate No. 3 with a 135 nm film and contact angle of $\theta = 110 \pm 1.1°$. For the No. 4 substrate, a self-assembly monolayer of trichloro (1H,1H,2H,2H-perfluorooctyl)-silane was coated on the copper plate using chemical vapor deposition, rendering its contact angle $\theta = 104 \pm 0.7°$. The No. 5 substrate corresponded to an uncoated polished copper plate with $\theta = 62 \pm 0.9°$. To vary the wettability of the substrates, we applied the oxygen plasma treatment to copper plates for 30 s and 300 s, respectively, yielding the No. 6 and No. 7 substrates with $\theta = 33 \pm 0.8°$ and $\theta = 22 \pm 0.6°$. We had verified that a surface with such oxygen plasma treatment can maintain its wettability within 30 min while one single impact experiment took around 2 min. Thus, we can ensure that the surface wettability was valid during experiments.

We used the confocal microscopy (Leica DCM8) to measure the surface roughness and thickness of a PTFE film. Supplementary Fig. 2a shows a representative topography image of a PTFE coated substrate, indicating its surface roughness. The thickness was determined by the height difference between the coated and uncoated sides of the substrate (see Supplementary Fig. 2b).

Experimental procedure. We conducted the experiments in a closed chamber enclosing a customized cryostage. A room-temperature deionized water droplet with a diameter of $D_0 = 2.2 - 3.4$ mm was generated by a syringe pump and then released above a cold copper substrate. To avoid frost formation on the substrate before droplet impacting, we filled the chamber with nitrogen gas. The impacting and freezing dynamics of droplets were recorded by a top and side high-speed camera (Phantom M310) at a frame rate of 5000 Hz. After a single impacting droplet was fully solidified, we applied a nitrogen gas flow at speed ~2 m s^{-1} to check whether it could be blown away due to complete self-peeling.

Data availability

References

1. Jung, S., Tiwari, M. K., Doan, N. V. & Poulikakos, D. Mechanism of supercooled droplet freezing on surfaces. *Nat. Commun.* **3**, 1–8 (2012).
2. Jung, S., Tiwari, M. K. & Poulikakos, D. Frost halos from supercooled water droplets. *Proc. Natl Acad. Sci. USA* **109**, 16073–16078 (2012).
3. Boreyko, J. B. & Collier, C. P. Delayed frost growth on jumping-drop superhydrophobic surfaces. *ACS Nano* **7**, 1618–1627 (2013).
4. Hou, Y. et al. Suppressing ice nucleation of supercooled condensate with biphilic topography. *Phys. Rev. Lett.* **120**, 075902 (2018).
5. Zhao, Y., Guo, Q., Lin, T. & Cheng, P. A review of recent literature on icing phenomena: Transport mechanisms, their modulations and controls. *Int. J. Heat. Mass Transf.* **159**, 120074 (2020).
6. Roisman, I. V. & Tropea, C. Wetting and icing of surfaces. *Curr. Opin. Colloid Interface Sci.* **53**, 101400 (2020).
7. Fang, W.-Z., Zhang, H., Zhang, C.-Y. & Yang, C. Freezing process of ferrofluid droplets: numerical and scaling analyses. *Phys. Rev. Fluids* **5**, 053601 (2020).
8. Mishchenko, L. et al. Design of ice-free nanostructured surfaces based on repulsion of impacting water droplets. *ACS Nano* **4**, 7699–7707 (2010).
9. Schremb, M., Roisman, I. V. & Tropea, C. Transient effects in ice nucleation of a water drop impacting onto a cold substrate. *Phys. Rev. E* **95**, 022805 (2017).
10. Wang, L., Kong, W., Wang, F. & Liu, H. Effect of nucleation time on freezing morphology and type of a water droplet impacting onto cold substrate. *Int. J. Heat. Mass Transf.* **130**, 831–842 (2019).
11. Marin, A. G., Enriquez, O. R., Brunet, P., Colinet, P. & Snoeijer, J. H. Universality of tip singularity formation in freezing water drops. *Phys. Rev. Lett.* **113**, 054301 (2014).
12. Schremb, M., Roisman, I. V. & Tropea, C. Normal impact of supercooled water drops onto a smooth ice surface: experiments and modelling. *J. Fluid Mech.* **835**, 1087 (2018).
13. Kant, P., Müller-Groeling, H. & Lohse, D. Pattern formation during the impact of a partially frozen binary droplet on a cold surface. *Phys. Rev. Lett.* **125**, 184501 (2020).
14. Graeber, G., Schutzius, T. M., Eghlidi, H. & Poulikakos, D. Spontaneous self-dislodging of freezing water droplets and the role of wettability. *Proc. Natl Acad. Sci. USA* **114**, 11040–11045 (2017).

15. Cao, L., Jones, A. K., Sikka, V. K., Wu, J. & Gao, D. Anti-icing superhydrophobic coatings. *Langmuir* **25**, 12444–12448 (2009).
16. Boreyko, J. B. & Chen, C.-H. Self-propelled dropwise condensate on superhydrophobic surfaces. *Phys. Rev. Lett.* **103**, 184501 (2009).
17. Kreder, M. J., Alvarenga, J., Kim, P. & Aizenberg, J. Design of anti-icing surfaces: smooth, textured or slippery? *Nat. Rev. Mater.* **1**, 1–15 (2016).
18. Golovin, K., Dhyani, A., Thouless, M. & Tuteja, A. Low–interfacial toughness materials for effective large-scale deicing. *Science* **364**, 371–375 (2019).
19. Miljkovic, N. et al. Jumping-droplet-enhanced condensation on scalable superhydrophobic nanostructured surfaces. *Nano Lett.* **13**, 179–187 (2013).
20. Shardt, N., Bigdeli, M. B., Elliott, J. A. & Tsai, P. A. How surfactants affect droplet wetting on hydrophobic microstructures. *J. Phys. Chem. Lett.* **10**, 7510–7515 (2019).
21. Bird, J. C., Dhiman, R., Kwon, H.-M. & Varanasi, K. K. Reducing the contact time of a bouncing drop. *Nature* **503**, 385–388 (2013).
22. Liu, Y. et al. Pancake bouncing on superhydrophobic surfaces. *Nat. Phys.* **10**, 515–519 (2014).
23. Gauthier, A., Symon, S., Clanet, C. & Quéré, D. Water impacting on superhydrophobic macrotextures. *Nat. Commun.* **6**, 1–6 (2015).
24. Maitra, T. et al. Supercooled water drops impacting superhydrophobic textures. *Langmuir* **30**, 10855–10861 (2014).
25. Zhang, R., Hao, P., Zhang, X. & He, F. Supercooled water droplet impact on superhydrophobic surfaces with various roughness and temperature. *Int. J. Heat. Mass Transf.* **122**, 395–402 (2018).
26. Gielen, M. V. et al. Solidification of liquid metal drops during impact. *J. Fluid Mech.* **883**, A32 (2020).
27. Zhang, X., Liu, X., Wu, X. & Min, J. Impacting-freezing dynamics of a supercooled water droplet on a cold surface: rebound and adhesion. *Int. J. Heat. Mass Transf.* **158**, 119997 (2020).
28. Xue, M., Chandra, S. & Mostaghimi, J. Investigation of splat curling up in thermal spray coatings. *J. Therm. Spray. Technol.* **15**, 531–536 (2006).
29. de Ruiter, J., Soto, D. & Varanasi, K. K. Self-peeling of impacting droplets. *Nat. Phys.* **14**, 35–39 (2018).
30. Kant, P., Koldeweij, R. B., Harth, K., van Limbeek, M. A. & Lohse, D. Fast-freezing kinetics inside a droplet impacting on a cold surface. *Proc. Natl Acad. Sci. USA* **117**, 2788–2794 (2020).
31. Kang, C., Sakaguchi, M., Amano, A., Kurokawa, Y. & Inoue, H. Quenching stress and fracture of paraffin droplet during solidification and adhesion on metallic substrate. *Surf. Coat. Technol.* **374**, 868–877 (2019).
32. Ghabache, E., Josserand, C. & Séon, T. Frozen impacted drop: from fragmentation to hierarchical crack patterns. *Phys. Rev. Lett.* **117**, 074501 (2016).
33. Song, D., Jiang, Y., Chou, T., Asawa, K. & Choi, C.-H. Spontaneous deicing on cold surfaces. *Langmuir* **36**, 11245–11254 (2020).
34. Fang, W.-Z., Zhu, F., Tao, W.-Q. & Yang, C. How different freezing morphologies of impacting droplets form. *J. Colloid Interface Sci.* **584**, 403–410 (2020).
35. Hu, M. et al. Frozen patterns of impacted droplets: from conical tips to toroidal shapes. *Phys. Rev. Fluids* **5**, 081601(R) (2020).
36. Thiévenaz, V., Josserand, C. & Séon, T. Retraction and freezing of a water film on ice. *Phys. Rev. Fluids* **5**, 041601(R) (2020).
37. Landy, M. & Freiberger, A. Studies of ice adhesion: I. adhesion of ice to plastics. *J. Colloid Interface Sci.* **25**, 231–244 (1967).
38. Makkonen, L. Ice adhesion –theory, measurements and countermeasures. *J. Adhes. Sci. Technol.* **26**, 413–445 (2012).
39. Beeram, P. S. R. *Characterization of Ice Adhesion Strength Over Different Surfaces Pertinent to Aircraft Anti-/De-Icing*. Ph.D. thesis, (2017).
40. Schulson, E. M. & Duval, P. *Creep and Fracture of Ice* (2009).
41. Zhevnenko, S. Interfacial free energy of cu-co solid solutions. *Metall. Mater. Trans. A* **44**, 2533–2538 (2013).
42. Lee, J.-E. & Kim, H.-K. Self-cleanable, waterproof, transparent, and flexible ag networks covered by hydrophobic polytetrafluoroethylene for multi-functional flexible thin film heaters. *Sci. Rep.* **9**, 1–11 (2019).
43. Meuler, A. J. et al. Relationships between water wettability and ice adhesion. *ACS Appl. Mater. Interfaces* **2**, 3100–3110 (2010).
44. Barron, R. F. & Barron, B. R. *Design for Thermal Stresses* (John Wiley & Sons, 2011).
45. Clanet, C., Béguin, C., Richard, D. & Quéré, D. Maximal deformation of an impacting drop. *J. Fluid Mech.* **517**, 199 (2004).
46. Tsai, P., Hendrix, M. H., Dijkstra, R. R., Shui, L. & Lohse, D. Microscopic structure influencing macroscopic splash at high weber number. *Soft Matter* **7**, 11325–11333 (2011).
47. Thiévenaz, V., Séon, T. & Josserand, C. Freezing-damped impact of a water drop. *EPL (Europhys. Lett.)* **132**, 24002 (2020).
48. Varanasi, K. K., Deng, T., Smith, J. D., Hsu, M. & Bhate, N. Frost formation and ice adhesion on superhydrophobic surfaces. *Appl. Phys. Lett.* **97**, 234102 (2010).
49. Sarshar, M. A., Song, D., Swarctz, C., Lee, J. & Choi, C.-H. Anti-icing or deicing: icephobicities of superhydrophobic surfaces with hierarchical structures. *Langmuir* **34**, 13821–13827 (2018).
50. Pasandideh-Fard, M., Pershin, V., Chandra, S. & Mostaghimi, J. Splat shapes in a thermal spray coating process: simulations and experiments. *J. Therm. Spray. Technol.* **11**, 206–217 (2002).

Acknowledgements

Author contributions

W.Z.F., F.Z., and C.Y. designed the research; W.Z.F. and F.Z. conducted the research; W.Z.F., F.Z., and L.Z. performed the analysis; C.Y., L.Z., and W.Q.T supervised the research; W.Z.F., L.Z., and C.Y. led the writing.

Competing interests

The authors declare no competing interests.

Additional information

Supplementary information The online version contains supplementary material available at https://doi.org/10.1038/s42005-022-00827-0.

Correspondence and requests for materials should be addressed to Lailai Zhu or Chun Yang.

Peer review information *Communications Physics* thanks the anonymous reviewers for their contribution to the peer review of this work. Peer reviewer reports are available.

Reprints and permission information is available at http://www.nature.com/reprints

Publisher's note Springer Nature remains neutral with regard to jurisdictional claims in published maps and institutional affiliations.